Journal of Materials Science: Materials in Electronics (2018) 29:19043–19051
https://doi.org/10.1007/s10854-018-0030-0

Microstructure and electrical properties of $K_{0.5}Na_{0.5}NbO_3$ lead-free piezoelectric ceramics sintered in low pO_2 atmosphere

Zi-de Yu[1] · Xiao-ming Chen[1] · Han-li Lian[2] · Qian Zhang[1] · Wen-xin Wu[1]

Received: 30 June 2018 / Accepted: 6 September 2018 / Published online: 8 September 2018

Abstract
Pure $K_{0.5}Na_{0.5}NbO_3$ lead-free piezoelectric ceramics without any dopants/additives were sintered at various temperatures (950–1125 °C) in low pO_2 atmosphere ($pO_2 \sim 10^{-6}$ atm). All ceramics exhibit high relative densities (> 94%) and low weight loss (< 0.6%). Compared to the ceramics sintered in air, the ceramics sintered in low pO_2 exhibit improved electrical properties. The piezoelectric constant d_{33} and converse piezoelectric constant d_{33}* are 112 pC/N and 119 pm/V, respectively. The ceramics show typical ferroelectric behavior with the remnant polarization of 21.6 μC/cm^2 and coercive field of 15.5 kV/cm under measurement electric field of 70 kV/cm. The good electrical properties of the present samples are related to the suppression of volatility of the alkali cations during the sintering process in low pO_2 atmosphere.

1 Introduction

Recently, lead-free piezoelectric materials such as potassium niobate-based ceramics have been studied because of the increased environmental concern [1–4]. Among them, potassium sodium niobate (KNN)-based ceramics are widely investigated due to their good piezoelectric properties and high Curie temperature (~420 °C) [5–7]. However, it is hard to obtain dense KNN-based ceramics by means of conventional sintering methods [5, 8]. In addition, the temperatures for sintering KNN-based ceramics are always higher than 1000 °C, causing heavy loss of alkali elements and consequent compositional fluctuation [5, 9]. The formation of Na^+/K^+ vacancies in the KNN-based ceramics caused by Na^+/K^+ loss during the sintering process strongly affects their electrical properties [10–12]. Pure KNN ceramics without any dopants/additives always have low piezoelectric constant d_{33} (80 pC/N) [13, 14]. In order to improve piezoelectric properties, various methods were applied. Satio et al. prepared textured KNN ceramics and obtained high d_{33} (416 pC/N) [15]. Wu et al. reported very high d_{33} values of KNN-based ceramics by designing phase boundaries [4]. Special sintering techniques can also facilitate improving ferroelectric and piezoelectric properties of KNN-based ceramics. Li et al. sintered KNN ceramics with d_{33} value of 148 pC/N by using spark plasma sintering [16]. Jaeger et al. reported that the hot-pressed KNN ceramics exhibited relative densities higher than 99% and d_{33} as high as 160 pC/N [17]. In our previous work, we prepared the pure KNN ceramic with fine grains (~0.1 μm) and good ferroelectric properties [18].

Low partial pressure of oxygen (pO_2) is one of important reduced atmospheres for sintering dielectric and piezoelectric materials. Tsuji et al. sintered $SrTiO_3$-based colossal permittivity barrier layer capacitors in pO_2 as low as 10^{-13} atm [19]. Kobayashi et al. sintered KNN–LiF ceramics in low pO_2 atmosphere and obtained higher resistivity [20]. Huan et al. obtained SnO_2 and ZrO_2 co-modified KNN ceramics with enhanced piezoelectric properties by firing under reduced atmosphere [21]. Co-fired KNN-based multilayer materials with inner nickel/copper electrodes could be prepared in low pO_2 atmospheres [22–24]. Shimizu et al. have reported that sintering in the low pO_2 atmosphere could suppress the volatilization of Na^+ in the $NaNbO_3$ system [25]. The theoretical analysis points out that the activation energy of volatilization of cations increases remarkably in reduced atmospheres, and thus the loss of alkali elements could be decreased obviously [26].

✉ Xiao-ming Chen
xmchen@snnu.edu.cn

[1] School of Physics and Information Technology, Shaanxi Normal University, Xi'an 710119, People's Republic of China

[2] School of Science, Xi'an University of Posts and Telecommunications, Xi'an 710121, People's Republic of China

In this study, the low pO_2 firing system was built and pure $K_{0.5}Na_{0.5}NbO_3$ ceramics without any dopants/additives were prepared via the solid-state reaction method. The ceramics were sintered in low pO_2 atmosphere. Microstructure, dielectric, piezoelectric and ferroelectric properties of the ceramics were studied in detail.

2 Experimental procedures

The composition of $K_{0.5}Na_{0.5}NbO_3$ (KNN) ceramics without any dopants/additives was chosen. The raw materials were Na_2CO_3 (99.95%), K_2CO_3 (99.0%), and Nb_2O_5 (99.9%) powders (Alfa Aesar). After drying, the raw powders were weighed out and then ball-milled for 24 h in ethanol. The calcination temperature was 900 °C, and the dwelling time was 3 h. Both the heating and cooling rates are 180°C/h. After calcination, the obtained powders were milled again for 12 h. Pellets with diameter of 12 mm were pressed, and followed by a cold-isostatic pressing under 200 MPa. The pellets were sintered in reduced atmosphere with $pO_2 \sim 10^{-6}$ atm. The sintering temperatures were changed from 950 to 1125 °C. The low pO_2 firing system is schematically shown in Fig. 1a. Figure 1b exhibits the photograph of the low pO_2 firing system in the lab. The pO_2 sintering system is comprised of a tube furnace (GSL-1500X, MTI Corporation, China), a digital flow meter with four gas flow controllers (Mass-Flo Controller, MKS Type 247, USA), and four valves. The pO_2 within the furnace is established by the equilibrium of water vapor and hydrogen. The water vapor is carried into the furnace by the N_2 (#4, in Fig. 1a). The dew temperature can be adjusted by water bath on a thermostatically controlled heater (DF-101S, Zhengzhou Greatwall Sci. Ind. Trade Co. Ltd, China). At the exhaust end, the gas is drained into the atmosphere through a bottle containing oil. By changing the flow rates of dry N_2/H_2 (95/5 vol% ratio) mixing gas, dry N_2 gas, and wet N_2 gas (dew), the pO_2 values in the tube furnace can be tuned, which were measured by using a ZrO_2 oxygen sensor (Oxyprobe; Australian Oxytrol System Pty Ltd.). For example, as the samples were sintered at 1075 °C, the gas flow contained 5 cc/min of 5% H_2/95% N_2 gas, 45 cc/min of dry N_2, and 450 cc/min of N_2 through ion-free water at 60 °C. The valve of air gas (#1, in Fig. 1a) is always closed during the low pO_2 sintering process.

Microstructures were observed via a scanning electron microscope (SEM, Nova Nano 450). The size distribution of grains in the ceramics was determined from more than 200 particles in each sample using Nano Measurer software. Crystallite structure was investigated via X-ray diffraction (XRD, Rigaku D/Max 2550) using CuK_α radiation. For electrical characterization, silver electrodes were coated on the surfaces of the polished ceramics and fired at 650 °C for 0.5 h. Dielectric properties were measured by means of a precision Agilent E4980A LCR meter. The ceramics were poled in silicone oil bath at 80 °C and 40 kV/cm for 15 min. Piezoelectric constant (d_{33}) was measured via a quasistatic d_{33} meter (ZJ-4A). Impedance properties were measured via a broadband dielectric spectrometer (Concept 80, Novocontrol Tech.). Ferroelectric properties were measured via a Radiant ferroelectric testing apparatus (Radiant Technologies Inc.).

3 Results and discussion

The weight loss (*WL*) of the ceramics is important in reflecting the volatilization of alkali elements. In order to obtain the *WL* values of the ceramics during sintering, four pellets were put in an Al_2O_3 crucible before sintering. They were baked at 120 °C for over 24 h to remove moisture. After baking, they were immediately weighed using an electronic balance (XT220A, Precisa, Switzerland) and the value of $(m_{\text{crucible}} + m_{0-4})$ was obtained, in which m_{crucible} is the mass of the crucible and m_{0-4} is the mass of the four pellets before sintering. After sintering, the same crucible and four samples were weighed together again and the value of $(m_{\text{crucible}} + m_{1-4})$ was obtained, in which m_{1-4} is the mass of the four pellets after sintering. Then, the weight loss of the ceramics during sintering was calculated according to the following equation:

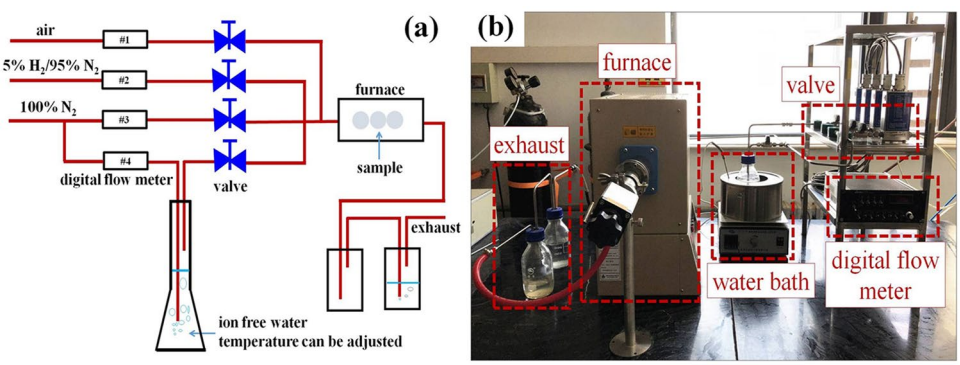

Fig. 1 **a** The schematic diagram of low pO_2 sintering system; **b** the photographs of low pO_2 sintering system

$$WL = [(m_{\text{crucible}} + m_{0-4}) - (m_{\text{crucible}} + m_{1-4})]/m_{0-4} \times 100\%. \quad (1)$$

It should be mentioned that no any binder was added in the pellets and no powders were used during sintering. It was found that the mass of the crucible did not change after sintering. By means of the same method, one pellet was used to measure weight loss and the obtained *WL* value is very similar as that obtained via the four samples. It is reasonable that the obtained *WL* values are the full weight loss during the sintering. The values of weight loss and relative densities of the ceramics sintered in low pO_2 atmosphere as a function of sintering temperatures are shown in Fig. 2. All ceramics exhibit relative densities higher than 94%. As the $K_{0.5}Na_{0.5}NbO_3$ ceramics were sintered in air, the relative densities are only around 88% [18]. The weight loss increases slowly as the sintering temperature increases. For the sintering temperatures between 950 and 1125 °C, the weight loss of the ceramics is very low (< 0.6%), which is lower than the values of the KNN-based ceramics sintered in flowing O_2 [27] and air [28]. As the samples were sintered in air, alkali cations can volatilize easily, as shown via the Kröger–Vink equation:

$$2A_A^{\times} + \frac{1}{2}O_O^{\times} \leftrightarrow A_2O(\uparrow) + 2V_A' + V_O^{\cdot\cdot}, \quad (2)$$

where A contains Na and K elements. The theoretical analysis points out that the activation energy of volatilization of cations increases remarkably in reduced atmospheres [26]. Thus, the sintering in low pO_2 atmosphere can suppress volatilization of the alkali cations, resulting in low weight loss.

The SEM image of the thermally etched ceramic sintered in low pO_2 and at 1075 °C is shown in Fig. 3a. The ceramic exhibits dense microstructure, corresponding to the high relative density (~95%). The grains show square

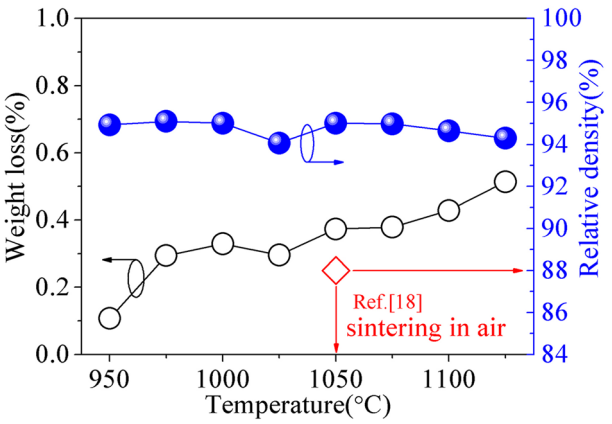

Fig. 2 The weight loss and relative density of the ceramics as function of sintering temperatures

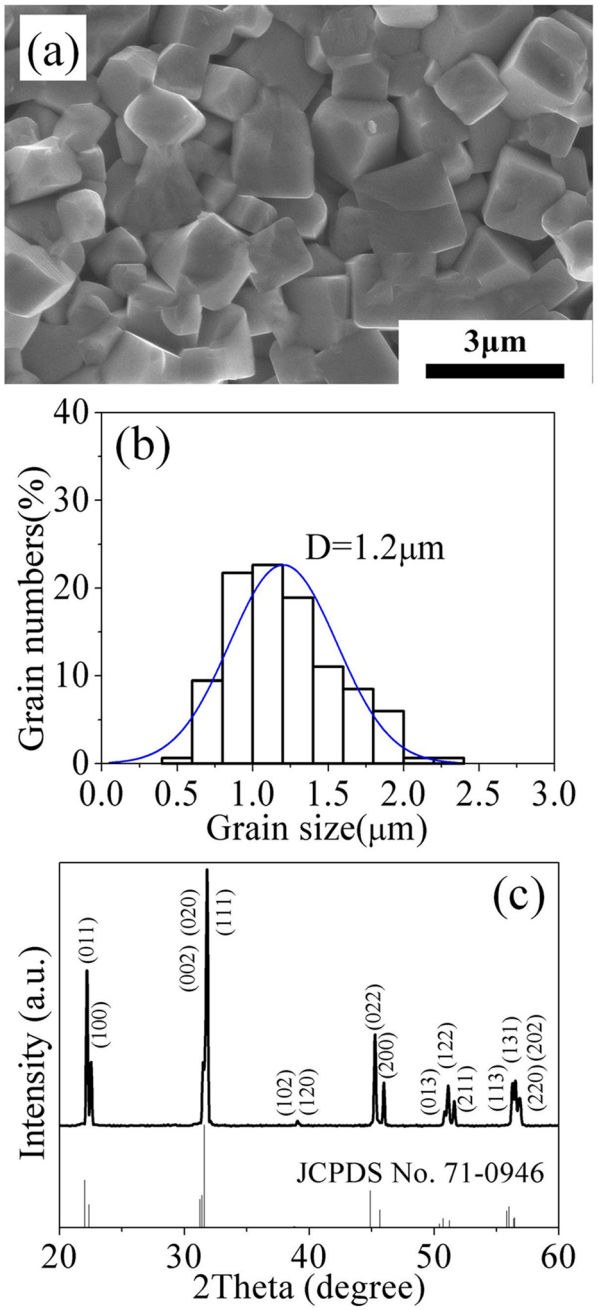

Fig. 3 **a** The SEM image of the ceramic sintered in low pO_2 atmosphere and at 1075 °C; **b** size distribution of the grains in the ceramic; **c** XRD curve of the ceramic

shape, which is similar to those in the ceramics sintered in air [29]. The grain size distribution of the ceramic is shown in Fig. 3b. The mean grain size is approximate 1.2 μm. The $K_{0.5}Na_{0.5}NbO_3$ ceramics sintered in air via the conventional solid-state reaction method using the similar synthesis parameters have the mean size of 2 μm [30]. Compared to the sintering atmosphere of air, the sintering atmosphere of low pO_2 decreased grain sizes of the ceramics, as the

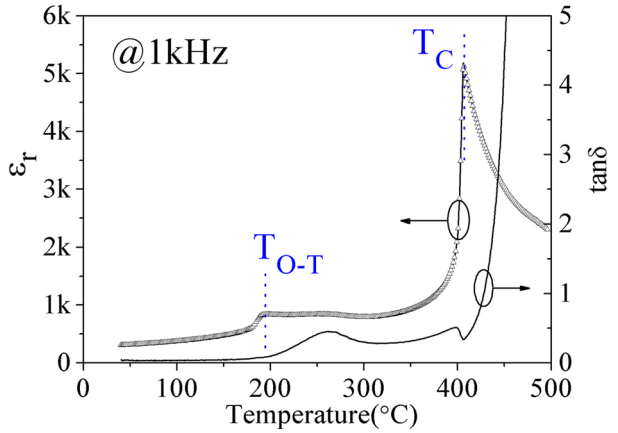

Fig. 4 Changes of ε_r and tan δ vs. temperature at 1 kHz

$NaNbO_3$ system reported by Shimizu et al. [25]. The XRD curve of the ceramic sintered at 1075 °C is shown in Fig. 3c. The XRD peaks can be well indexed with the orthorhombic symmetry (PDF no. 710946), with no secondary phase detected. In the following study, the ceramics sintered at 1075 °C were chosen to study the electrical properties.

Figure 4 shows the temperature dependences of dielectric loss (tan δ) and dielectric constant (ε_r) of the ceramic measured at 1 kHz. The $\varepsilon_r - T$ curve exhibits two dielectric anomalies, corresponding to the phase transitions of tetragonal-cubic around T_C and orthorhombic-tetragonal around T_{O-T}, respectively. The values of tan δ, ε_r, T_C and T_{O-T} are 0.04, 366, 406 °C, and 195 °C, respectively. The corresponding values of the ceramics sintered in air are 0.46, 183, 400 °C, and 191 °C, respectively [18]. Compared to the sintering atmosphere of air, the low pO_2 sintering atmosphere facilitates increasing ε_r, decreasing tan δ, and increasing phase transition temperatures.

The curves of alternating-current conductivity (σ'_{ac}) vs. frequency measured at the given temperatures are shown in Fig. 5a. σ'_{ac} is closely related to temperature and frequency. Two regions are distinguished denoted as Region A and Region B. Plateau appears in Region A at frequencies between 10^{-1} Hz and approximate 10^5 Hz. The plateau range in Region A depends on the temperature. With increasing temperature, the conductivity increases and the plateau region extends towards higher frequency direction. In Region B, the dependence of conductivity on temperature decreases and the conductivity increases rapidly with increasing frequency. The change of σ'_{ac} with frequency can be fitted via the universal law, as shown in Eq. (3) [31]:

$$\sigma'_{ac} = \sigma_{dc} + \sigma_0 f^n, \tag{3}$$

where σ_{dc} is direct-current (DC) conductivity, σ_0 is the temperature dependent constant, f is frequency. The n values are temperature and frequency dependent and always

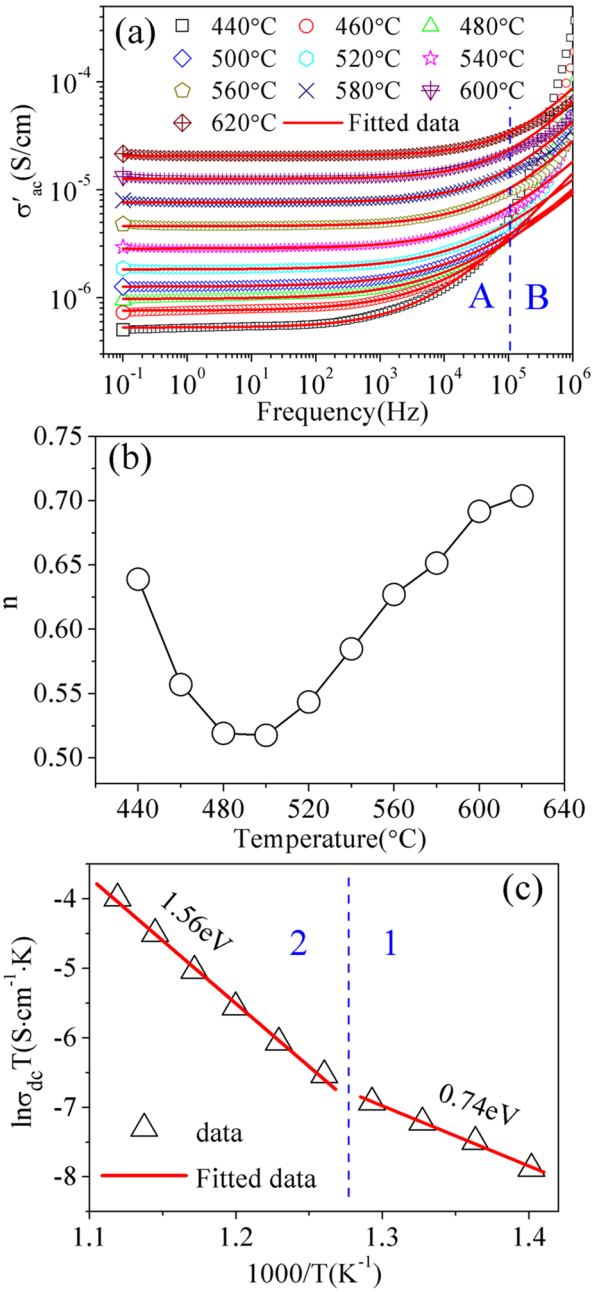

Fig. 5 **a** Variation of AC conductivity with frequency at given temperatures. The solid lines show fitting lines. **b** The obtained n values. **c** Variation of ln σ_{dc} T vs. $1/T$

between 0 and 1. The σ'_{ac} data were fitted via Eq. (3) and are shown in Fig. 5a. The obtained n values are shown in Fig. 5b. The n values decrease to a minimum and then increase with temperature increasing. The similar phenomenon was observed in other systems, such as $Na_{0.5}Bi_{2.5}Nb_2O_9$ [32], $(Na_{0.5}Bi_{0.5})_{0.91}Ba_{0.09}TiO_3$ [33], $SrNiP_2O_7$ [34] and $Bi_{0.90}La_{0.10}Fe_{0.95}Mn_{0.05}O_3$ [35]. Conduction activation

energy (E_a) was calculated according to the Arrhenius equation:

$$\sigma_{dc} = \frac{\sigma_0}{T} \exp\left(-\frac{E_a}{k_B T}\right), \tag{4}$$

where k_B is Boltzmann constant, T is absolute temperature, σ_0 is the pre-exponential term. The fitting results are shown in Fig. 5c. The plots exhibit a convex knee between the low temperature and high temperature regions. The two regions show the different E_a values. The E_a values are 0.74 eV and 1.56 eV in the low-temperature range (Range 1) and high-temperature range (Range 2), respectively. The E_a value in Range 1 is smaller than that in Range 2. The different E_a values in the different temperature ranges imply a change in conduction mechanism [26, 36, 37].

The complex impedance plots (Z'–Z'') of the ceramic measured at the different temperatures are shown in Fig. 6a. The magnification of Z'–Z'' plots in the high frequency range is shown in Fig. 6b. The plots do not exhibit typical single semicircles, implying non-Debye-type relaxation mechanism [38]. The impedance decreases with increasing temperature. A tail appears in the side of low frequency. According to the brick-layer model, the impedance should be depicted via capacitance and resistance from grain boundaries and grains, respectively [39]. As shown in Fig. 6a, b, the centers for all semicircles arcs are below the Z' axis. The constant phase element (CPE) should be introduced in the equivalent circuit, and the complex impedance (Z^*) can be expressed as following [40, 41]:

$$Z^* = Z' - iZ'', \tag{5}$$

$$Z^* = \frac{R_g}{1 + i\omega R_g C_g} + \frac{R_{gb}}{1 + R_{gb}A(i\omega)^{\beta}}, \tag{6}$$

$$Z_{CPE} = 1/Y_{CPE} = 1/A(i\omega)^{\beta}, \tag{7}$$

where i is imaginary number and $i^2 = -1$; R_g and C_g are resistance and capacitance from grains, respectively; R_{gb} and C_{gb} are resistance and capacitance from grain boundaries, respectively; ω is the angular frequency; Y_{CPE} is the admittance of CPE; A and β are constants. The parameter β is between 0 and 1. $\beta = 1$ is for ideal capacitor and $\beta = 0$ is for ideal resistor. The experimental data were fitted with the equivalent circuit using the ZVIEW software according to Eq. (6). The fitting results are shown in Fig. 6a, b, and the equivalent circuit is shown in the inset of Fig. 6a. The parameters R_g, R_{gb} and β were obtained and shown in Fig. 6c. With increasing temperature, the values of β, R_{gb}, and R_g decrease. In the low-temperature range (Range 1), the R_{gb} and R_g values decrease rapidly. In the high-temperature range (Range 2), the R_{gb} and R_g values decrease slowly (Fig. 6c). The decreasing slope of β is contrary to that of R_{gb} and R_g. The parameter β is between 0.79 and 0.95, implying non-Debye-type relaxation mechanism. For the studied temperatures, the R_{gb} values are larger than R_g values.

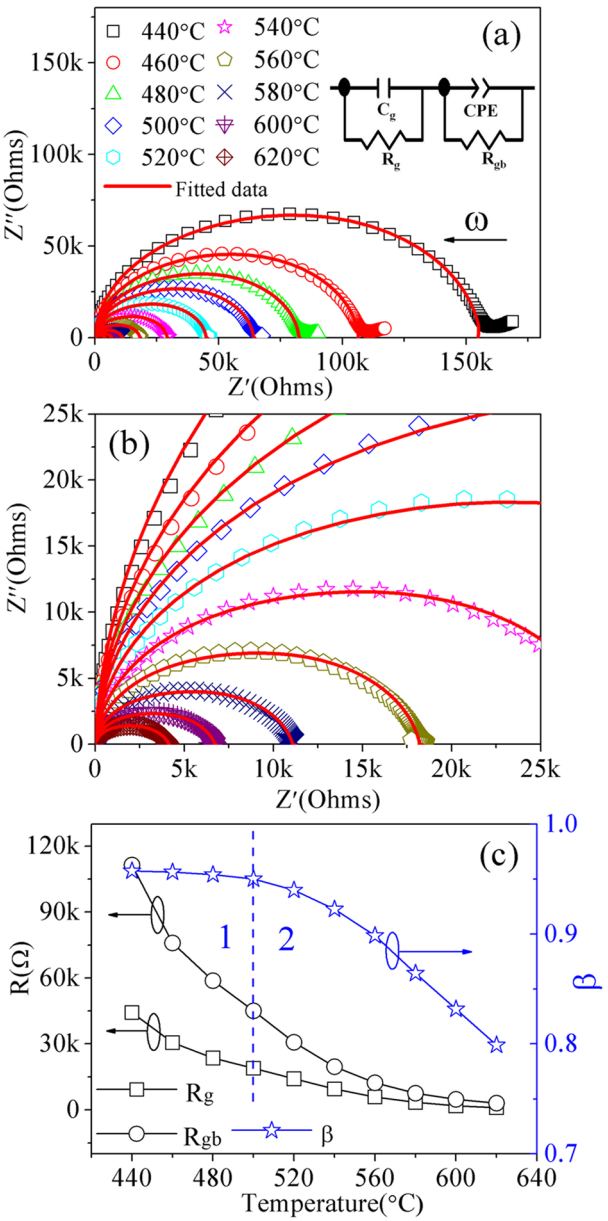

Fig. 6 **a** Variation of Z'' vs. Z' of the ceramics at given temperatures. **b** The magnification of the Z'' ~ Z' at high frequencies. The solid lines in **a, b** are fitted curves. **c** The obtained R_{gb}, R_g and β values

The polarization–electric field (P–E) hysteresis loops of the ceramic measured under different electric fields between 40 and 70 kV/cm are shown in Fig. 7a. The coercive field (E_c) and remnant polarization (P_r) values are shown in Fig. 7b. The sample exhibits typical P–E hysteresis loops. With increasing the measurement electric fields, the P–E loops tend to be saturated. The values of P_r and E_c measured at 70 kV/cm are 21.6 μC/cm^2 and 15.5 kV/cm, respectively.

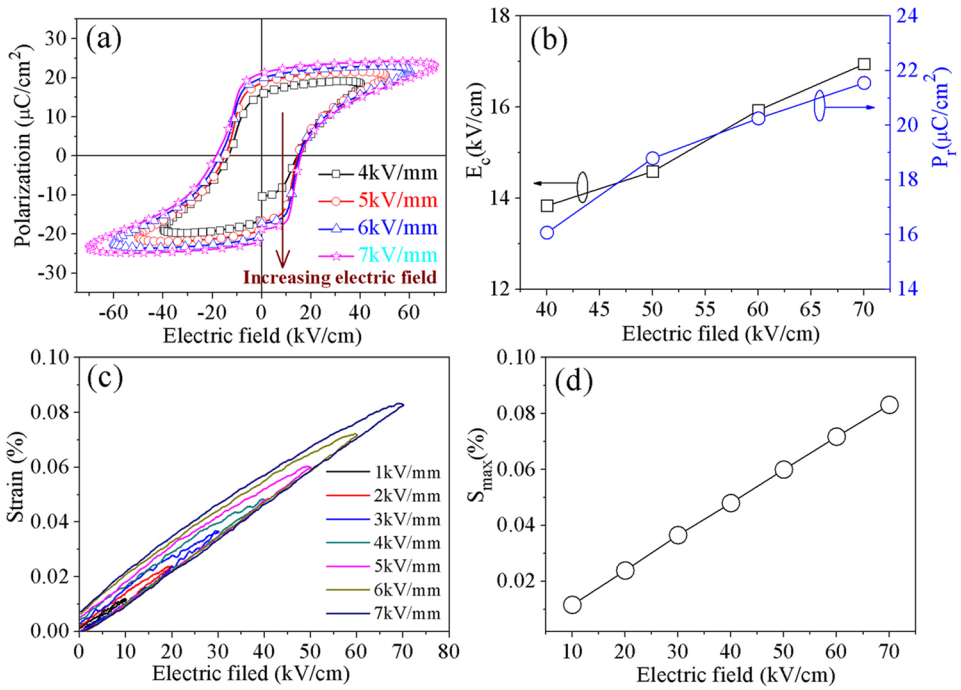

Fig. 7 **a** Typical *P–E* loops and **c** *S–E* curves under various applied electrical fields measured at 1 Hz at room temperature. **b, d** The values of E_c, P_r, and S_{max} at the different applied electrical fields

For the $K_{0.5}Na_{0.5}NbO_3$ ceramic sintered in air, the values of P_r and E_c measured at 70 kV/cm are 17.5 μC/cm^2 and 6.5 kV/cm, respectively [18]. The sample sintered in low pO_2 atmosphere exhibits higher P_r and E_c. The curves of unipolar strain vs. electric field (*S–E*) measured at the different electric fields are shown in Fig. 7c. The sample exhibits typical strain curves. Unipolar strain increases with increasing electric field. The maximum values of strain (S_{max}) under the given electric fields are shown in Fig. 7d. The S_{max} value measured at 70 kV/cm is 0.083%. The converse piezoelectric coefficient (d_{33}^*) calculated via the following equation:

$$d_{33}^* = S_{\max}/E_{\max}, \tag{8}$$

where E_{max} and S_{max} is the maximum electric field and maximum strain according to the *S–E* curves, respectively. The d_{33}^* value measured at 70 kV/cm is 119 pm/V. The piezoelectric constant d_{33} is 112 pC/N. The ceramics with the same composition sintered in air exhibit lower d_{33} values [18, 42, 43]. Here, by sintering in the low pO_2 atmosphere, one can obtain the $K_{0.5}Na_{0.5}NbO_3$ ceramic with relatively high d_{33} value.

The Rayleigh law was utilized to study the nonlinear contribution of non-180° domain wall motion to piezoelectric properties as following [44–46]:

$$\varepsilon_r'(E_0) = \alpha E_0 + \varepsilon_{init}', \tag{9}$$

where α is the Rayleigh coefficient; ε'_{init} is a field-independent term, which represents a combination of the intrinsic ionic response together with the contribution from reversible domain wall vibration; E_0 is the amplitude of the electric field; $\varepsilon_r'(E_0)$ is the real part of ε_r under the E_0. By measuring *P–E* loops under various AC electric fields, one can calculate $\varepsilon_r'(E_0)$ as following:

$$\varepsilon_r'(E_0) = \sqrt{\varepsilon_r^2 + \varepsilon''_r{}^2} = \sqrt{(P_{p-p}/2\varepsilon_0 E_0)^2 - (A/\pi\varepsilon_0 E_0^2)^2}, \tag{10}$$

where ε_0 is vacuum dielectric constant, P_{p-p} is the value of polarization from *P–E* loop peak to peak, and A is *P–E* loop area. The extrinsic contribution (Con_{ex}) can be estimated as following:

$$Con_{ex} = \alpha E_0/(\alpha E_0 + \varepsilon'_{init}). \tag{11}$$

For Rayleigh analysis, the amplitude of the applied electrical field should be below 1/3 E_c ~ 1/2 E_c [44, 47]. Figure 8a shows the *P–E* loops measured under the various applied electrical fields (Here, the electrical field amplitude is below 8 kV/cm). The calculated $\varepsilon_r'(E_0)$ values under the different E_0 values are shown in Fig. 8b. The ε'_{init} and α values can be obtained by means of linear fitting according to Eq. (9). The $\varepsilon_r'(E_0)$ values under the different E_0 values can be well fitted by the linear fitting (Fig. 8b). The obtained values of α and ε'_{init} are 14.9×10^7 m^2/V^2 and 305.7, respectively. The Con_{ex} values at different E_0 values were calculated and are shown in Fig. 8b. The Con_{ex} values increase with increasing measured electric field, indicating that more domains switch under higher electric fields.

Grain size and electrical properties of the pure $K_{0.5}Na_{0.5}NbO_3$ ceramics sintered in air via the conventional solid-state reaction method are compared to those

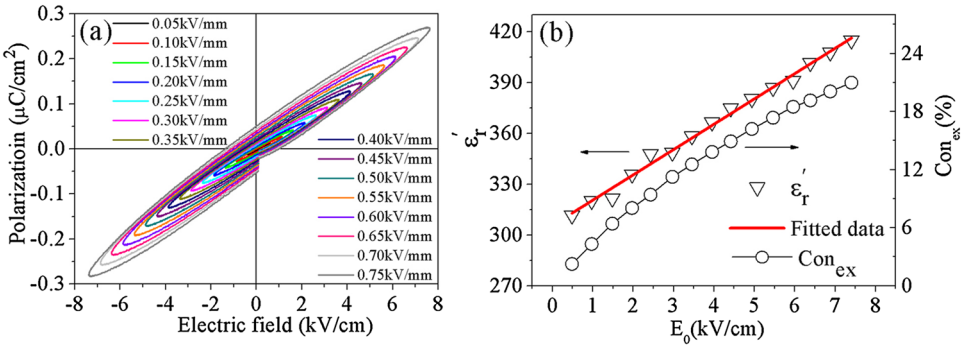

Fig. 8 **a** Typical *P*–*E* loops under various applied low electric fields. **b** The calculated $\varepsilon_r'(E_0)$ and Con_{ex} values under different E_0

of the present sample in Table 1. The ceramic sintered in low pO_2 atmosphere shows smaller grains (~ 1.2 μm) compared to those sintered in air (> 2 μm). Compared to the sintering atmosphere of air, the sintering atmosphere of low pO_2 can decrease grain size of the ceramics, which is related to the variation of point defects in the ceramics [25]. The decrease in grain size is very important because of the miniaturization of electronic devices. The sintering atmosphere of low pO_2 provides an optional route for decreasing size of grains in ceramics. The present sample exhibits higher P_r, d_{33}, and d_{33}^* values. The Q_m and k_p values of the present sample are 143 and 0.29, respectively. Compared to the doped KNN ceramics (Table 1), the present samples without any dopants/additives exhibit similar properties. By sintering in low pO_2 atmosphere, the $K_{0.5}Na_{0.5}NbO_3$ ceramics with small grains and good electrical properties were obtained. As is well known, one of the main problems for sintering KNN-based materials is volatility of alkali species in sintering process. The volatilization of K^+ and Na^+ causes the main problems of controlling stoichiometry and point defects in the ceramics, which is closely related to the electrical properties. As the samples were sintered in air, alkali cations could volatilize easily and point defects were introduced in the ceramics (Eq. 2). As mentioned above, activation energy of volatilization of cations increases remarkably in low pO_2 atmosphere, and so the loss of alkali elements could be suppressed obviously [26]. Thus, the ceramics sintered in low pO_2 atmosphere should have low defect concentration, which facilitates improving electrical properties. In this work, the weight loss of the pure $K_{0.5}Na_{0.5}NbO_3$ ceramics during the sintering process is very low (~ 0.6%), which is lower than the values of the KNN-based ceramics sintered in flowing O_2 and air [27, 28]. The low-pO_2-sintered $K_{0.5}Na_{0.5}NbO_3$ ceramics show better electrical properties in comparison with air-sintered $K_{0.5}Na_{0.5}NbO_3$ ceramics. The improved electrical properties of the ceramics are related to the dense microstructure and suppression of the alkali vacancies formation, as reported by others [25]. Here, by means of sintering in low pO_2 atmosphere, pure $K_{0.5}Na_{0.5}NbO_3$ ceramics with excellent electrical properties were obtained. The results demonstrate that the low pO_2 atmosphere is good for sintering KNN-based materials. But, it should be mentioned that the pO_2 values in the sintering process can affect the contents of oxygen vacancies and electrons in the materials [26]. The sintering in low pO_2 atmosphere can cause oxygen vacancies intrinsically, as shown via the following equation:

$$O_O^{\times} \leftrightarrow V_O^{\cdot\cdot} + 2e' + \frac{1}{2}O_2(\uparrow). \tag{12}$$

Table 1 Comparison of the $K_{0.5}Na_{0.5}NbO_3$ (KNN) ceramics between the sintering atmospheres of air and low pO_2

Samples	Sintering atmosphere	Grain Size (μm)	E_c (kV/cm)	P_r (μC/cm²)	d_{33} (pC/N)	d_{33}^* (pm/V)	Q_m	k_p	References
KNN	Air	1.2	6.5	17.5	60	–	–	–	[18]
KNN	Air	2	15.6[a]	16.3[a]	85	86[a]	–	–	[30]
KNN	Air	~3.9	8.5	11.4	96	–	–	0.28	[43]
KNN	Air	2.4	9.7	26	90	112	85	0.25	[48]
KNN	Low pO_2	1.2	16.9	21.6	112	119	143	0.29	This work
KNN–$LiNbO_3$	Air	2.5–3.0	–	18.8	120	104	–	–	[49]
KNN–$LiSbO_3$	Air	–	–	–	119	–	53	0.31	[50]
KNN–$LiTaO_3$	Air	6	–	15.5	132	–	–	0.29	[51]

The electrical properties of the doped KNN ceramics are also shown

[a]Estimated values from the curves in the references

The high concentration of oxygen vacancies and electrons may cause high electric conduction and deteriorate electrical properties of the ceramics. This is more serious in the case of very low pO_2 values. So, the sintering in the atmospheres with very low pO_2 values (such as lower than ~ 10^{-10} atm) is always followed by annealing in dry air or reduced atmosphere with relatively high pO_2 values (such as ~ 10^{-6} atm) [25]. In the present work, the pO_2 value during the sintering process was chosen as ~ 10^{-6} atm. The as-sintered samples without annealing exhibit good electrical properties. It can be expected that by changing pO_2 values, the electrical properties of the KNN-based ceramics can be tuned. The further studies are going on and will be reported in future.

4 Conclusions

Pure $K_{0.5}Na_{0.5}NbO_3$ lead-free ceramics without any dopants/additives were sintered in the low pO_2 atmosphere. The obtained ceramics exhibit dense microstructure and small grains with mean size of 1.2 μm. Electrical properties of the present sample are better than those sintered in air. The $K_{0.5}Na_{0.5}NbO_3$ ceramic sintered in low pO_2 exhibits d_{33} of 112 pC/N, d_{33}^* of 119 pm/V, P_r of 21.6 μC/cm^2, E_c of 15.5 kV/cm, Q_m of 143, k_p of 0.29. The sintering in low pO_2 atmosphere can suppress volatilization of the alkali cations, which facilitates improving electrical properties of the ceramics.

Acknowledgements Xiao-ming Chen gratefully acknowledges assistance from Dr. Clive A. Randall at The Pennsylvania State University for setting up the low pO_2 sintering system. This work was supported by Shaanxi Province Science and Technology Foundation (2018JM1009), Fundamental Research Funds for the Central Universities (nos. GK201803017, 2017CSZ001), and National Innovation and Entrepreneurship Training Program for College Students (no. CX2018100).

References

1. C. Pascual-Gonzalez, G. Schileo, A. Khesro, I. Sterianou, D.W. Wang, I.M. Reaney, A. Feteira, J. Mater. Chem. C **5**, 1990 (2017)
2. C. Pascual-Gonzalez, G. Schileo, S. Murakami, A. Khesro, D.W. Wang, I.M. Reaney, A. Feteira, Appl. Phys. Lett. **110**, 172902 (2017)
3. T. Ibn-Mohammed, S.C.L. Koh, I.M. Reaney, A. Acquaye, D.W. Wang, S. Taylor, A. Genovese, Energy Environ. Sci. **9**, 3495 (2016)
4. J.G. Wu, D.Q. Xiao, J.G. Zhu, Chem. Rev. **115**, 2559 (2015)
5. J.F. Li, K. Wang, F.Y. Zhu, L.Q. Cheng, F.Z. Yao, J. Am. Ceram. Soc. **96**, 3677 (2013)
6. Y. Gao, J.L. Zhang, X.J. Zong, C.L. Wang, J.C. Li, J. Appl. Phys. **107**, 074101 (2010)
7. D.W. Wang, F. Hussain, A. Khesro, A. Feteira, Y. Tian, Q.L. Zhao, I.M. Reaney, J. Am. Ceram. Soc. **100**, 627 (2017)
8. B. Malič, J. Koruza, J. Hreščak, J. Bernard, K. Wang, J.G. Fisher, A. Benčan, Materials **8**, 8117 (2015)
9. Y. Huan, X.H. Wang, R.L. Gao, L.T. Li, J. Am. Ceram. Soc. **97**, 3524 (2014)
10. C.-W. Ahn, C.-S. Park, C.-H. Choi, S. Nahm, M.-J. Yoo, H.-G. Lee, S. Priya, J. Am. Ceram. Soc. **92**, 2033 (2009)
11. Y.H. Zhen, J.F. Li, J. Am. Ceram. Soc. **89**, 3669 (2006)
12. S.J. Zhang, H.J. Lee, C. Ma, X.L. Tan, J. Am. Ceram. Soc. **94**, 3659 (2011)
13. L. Egerton, J. Am. Ceram. Soc. **42**, 438 (1959)
14. B. Malic, J. Bernard, A. Bencan, M. Kosec, J. Eur. Ceram. Soc. **28**, 1191 (2008)
15. Y. Saito, H. Takao, T. Tani, T. Nonoyama, K. Takatori, T. Homma, M. Nakamura, Nature **432**, 84 (2004)
16. J.F. Li, K. Wang, B.P. Zhang, L.M. Zhang, J. Am. Ceram. Soc. **89**, 706 (2006)
17. R.E. Jaeger, L. Egerton, J. Am. Ceram. Soc. **45**, 209 (1962)
18. Y.L. Su, X.M. Chen, Z.D. Yu, H.L. Lian, D.D. Zheng, J.H. Peng, J. Mater. Sci. **52**, 2934 (2017)
19. K. Tsuji, W.T. Chen, H.Z. Guo, X.M. Chen, T.K. Lee, W.H. Lee, C.A. Randall, RSC Adv. **6**, 92127 (2016)
20. K. Kobayashi, Y. Doshida, Y. Mizuno, C.A. Randall, J. Am. Ceram. Soc. **95**, 2928 (2012)
21. Y. Huan, X.H. Wang, T. Wei, P.Y. Zhao, J. Xie, Z.F. Ye, L.T. Li, J. Eur. Ceram. Soc. **37**, 2057 (2017)
22. S. Kawada, M. Kimura, Y. Higuchi, H. Takagi, Appl. Phys. Express **2**, 111401 (2009)
23. C. Liu, P. Liu, K. Kobayashi, C.A. Randall, J. Electroceram. **32**, 301 (2014)
24. L.S. Gao, S.W. Ko, H.Z. Guo, E. Hennig, C.A. Randall, J. Am. Ceram. Soc. **99**, 2017 (2016)
25. H. Shimizu, K. Kobayashi, Y. Mizuno, C.A. Randall, J. Am. Ceram. Soc. **97**, 1791 (2014)
26. R.J.D. Tilley, *Defect in Solids* (Wiley, Hoboken, 2008)
27. M. Matsubara, T. Yamaguchi, K. Kikuta, S.I. Hirano, Jpn. J. Appl. Phys. **44**, 258 (2005)
28. Z.Y. Shen, Y.H. Zhen, K. Wang, J.F. Li, J. Am. Ceram. Soc. **92**, 1748 (2009)
29. H.Q. Wang, Y.J. Dai, X.W. Zhang, J. Am. Ceram. Soc. **95**, 1182 (2012)
30. Z. Pan, J. Chen, L.L. Fan, J. Zhang, S.T. Zhang, Y. Huang, L.J. Lu, L. Fang, X.R. Xing, J. Am. Ceram. Soc. **98**, 3935 (2015)
31. G. Singh, V.S. Tiwari, P.K. Gupta, J. Appl. Phys. **107**, 064103 (2010)
32. Z.H. Peng, X.X. Zeng, F. Cao, X. Yang, J. Alloys Compd. **695**, 626 (2017)
33. K.S. Rao, B. Tilak, K.C.V. Rajulu, A. Swathi, H. Workineh, J. Alloys Compd. **509**, 7121 (2011)
34. M. Megdiche, C. Perrin-Pellegrino, M. Gargouri, J. Alloys Compd. **584**, 209 (2014)
35. J. Kolte, A.S. Daryapurkar, D.D. Gulwade, P. Gopalan, Ceram. Int. **4**, 12914 (2016)
36. Y.Z. Qiu, X.M. Chen, H.L. Lian, J.P. Ma, W.Q. Ouyang, Mater. Chem. Phys. **202**, 197 (2017)
37. T. Wang, X.M. Chen, Y.Z. Qiu, H.L. Lian, W.T. Chen, Mater. Chem. Phys. **186**, 407 (2017)
38. J.R. Macdonald, E. Barsoukov, *Impedance Spectroscopy: Theory, Experiment, and Applications*, 2nd edn. (Wiley, Hoboken, 2005), pp. 34–41
39. J. Fleig, J. Maier, J. Eur. Ceram. Soc. **19**, 693 (1999)
40. R.N. Bhowmik, K.A. Kumar, Mater. Chem. Phys. **177**, 417 (2016)
41. R.J. Tang, C. Jiang, J. Jian, Y. Liang, X. Zhang, H.Y. Wang, H. Yang, Appl. Phys. Lett. **106**, 022902 (2015)
42. K.P. Chen, J.Q. Zhou, F.L. Zhang, X.W. Zhang, C.W. Li, L.N. An, J. Am. Ceram. Soc. **98**, 1698 (2015)
43. X. Vendrell, J.E. García, X. Bril, D.A. Ochoa, L. Mestres, G. Dezanneau, J. Eur. Ceram. Soc. **35**, 125 (2015)

44. X.S. Qiao, X.M. Chen, H.L. Lian, W.T. Chen, J.P. Zhou, P. Liu, J. Am. Ceram. Soc. **99**, 198 (2016)
45. X.S. Qiao, X.M. Chen, H.L. Lian, J.P. Zhou, P. Liu, J. Eur. Ceram. Soc. **36**, 3995 (2016)
46. D.A. Hall, J. Mater. Sci. **36**, 4575 (2001)
47. R.E. Eitel, T.R. Shrout, C.A. Randall, J. Appl. Phys. **99**, 124110 (2006)
48. C. Liu, P. Liu, K. Kobayashi, W.G. Qu, C.A. Randall, J. Am. Ceram. Soc. **96**, 3120 (2013)
49. Y. Zhang, L.Y. Li, W.F. Bai, B. Shen, J.W. Zhai, B. Li, RSC Adv. **5**, 19647 (2015)
50. W. Yang, D.R. Jin, T.T. Wang, J.R. Cheng, Phys. B Condens. Matter **405**, 1918 (2010)
51. H.F. Hao, G.Q. Tan, H.J. Ren, A. Xia, P. Xiong, Ceram. Int. **40**, 9485 (2014)